Thermal Transport Through CTAB- and MTAB-Functionalized Gold Interfaces using Molecular Dynamics Simulations

Sydney A. Shavalier and J. Daniel Gezelter*

251 Nieuwland Science Hall, Department of Chemistry and Biochemistry, University of Notre Dame, Notre Dame, Indiana 46556

E-mail: gezelter@nd.edu

Abstract

Thermal transport coefficients, notably the interfacial thermal conductance, were determined in planar and spherical gold interfaces functionalized with CTAB (cetyltrimethylammonium bromide) or MTAB (16-mercapto-hexadecyl-trimethylammonium bromide) using reverse non-equilibrium molecular dynamics (RNEMD) methods. The systems of interest included (111), (110), and (100) planar facets as well as nanospheres ($r = 10$ Å). The effect of metal polarizability was investigated through the implementation of the density-readjusted embedded atom model (DR-EAM), a polarizable metal potential. We find that conductance is higher in MTAB-capped interfaces, due in large part to the metal-to-ligand coupling provided by the Au-S bond. Alternatively, CTAB does not couple strongly with either the metal or the solvent, and it is largely a barrier to heat transfer, resulting in a much lower interfacial thermal conductance. Through analysis of physical contact between the ligand and the solvent, we find that there is significantly more overlap in the MTAB systems than the CTAB systems, mirroring the trends we observed in the conductance.

Introduction

The choice of anti-aggregation agent is important in the synthesis of gold nanoparticles. One of the most widely-used surfactants, cetyltrimethylammonium bromide (CTAB), is an ionic surfactant that forms micelles in aqueous solutions and is thought to form bilayers surrounding gold nanoparticles. Abdullah *et al.* and Khan *et al.* separately determined that the size of gold nanoparticles can be tuned by altering the CTAB concentration during nanoparticle synthesis.[1,2]

Recent advances in biomedical applications of functionalized gold nanoparticles[3–6] have made the choice of nanoparticle surfactant particularly relevant. To be viable in a biological environment, the cytotoxicity of the ligand must generally be low. Sodium citrate[7–9] and some thiols[10–14] have been studied extensively as potentially safe ligands in biological environments. CTAB, however, is considered cytotoxic, as gold particles coated with this ligand induce cellular necrosis.[15,16] Nonetheless, Carnovale *et al.* determined that while spherical and prismatic gold nanoparticles functionalized with CTAB were cytotoxic, rod and cube-like structures capped with the same ligand were tolerated by the cells of interest.[17]

Another anti-aggregation agent with similar presentation to the aqueous solution is 16-mercapto-hexadecyl-trimethylammonium bromide (MTAB). Several studies have utilized MTAB-capped gold nanorods with no resulting cytotoxicity,[18–20] and MTAB can be used to displace citrate or CTAB molecules that are bound to gold nanoparticles.[21] An experimental study by Wu *et al.*[21] and a simulation study by Liang *et al.*[22] generally agreed on the structural behavior of MTAB ligands on gold nanoparticles of varying sizes. The ligand packing density on gold was found to mostly decrease with increasing particle size. Additionally, Vigderman *et al.* determined that MTAB-capped gold nanorods exhibited a higher cellular uptake *in vitro* than gold nanorods functionalized with polyethylene glycol.[19]

Photothermal therapies utilizing gold nanoparticles have been examined for their ability to effectively ablate tumor cells with minimal side effects for surrounding healthy tissue.[23] These therapies work by converting laser irradiation in the near-IR into heat via a plasmon resonance in the gold nanoparticles. Therefore, in addition to minimizing the cytotoxicity of an anti-aggregation

agent, understanding thermal transport from the gold particles through the ligand and into the surroundings will be important in synthesizing nanoparticles for these therapies.

An experimental study of heat transfer through CTAB-capped gold nanorods in water by Huang *et al.* found that the thermal conductivity of the CTAB bilayer decreases with increasing CTAB concentration, and that the thermal conductivity is dominated by the CTAB ligands rather than the surrounding water.[24] Using a benchmark for the rate of energy dissipation with sodium citrate as a ligand,[25] Nguyen *et al.*[26] found that when gold is capped with CTAB rather than sodium citrate, heat transfer time constants are larger in CTAB-capped gold even when the particles are the same size as those in the benchmark study.[25] They theorized that the differences in the rates of energy dissipation were from the increased thermal resistance provided by the longer CTAB chains.[26]

Salajkova *et al.* found that MTAB-capped gold nanorods were more thermally stable than gold capped with oligoethylene glycol molecules in an experimental study.[20] Given the utility that CTAB and MTAB have shown in these studies, a comprehensive examination of heat transfer through gold functionalized with either CTAB or MTAB is warranted.

One important question to address is the binding motif of both of these molecules on the surface of gold. For MTAB, the strong S-Au bond preferences the formation of monolayers, where the TAB^+ and Br^- are solvated in water, and the sulfur atom binds directly to the surface. For CTAB, the situation is less clear. Experiments by Kawasaki *et al.* probed the structural properties of CTAB near the gold surface.[27] They determined that CTAB forms a monolayer near the gold surface at low concentrations ([CTAB] $<$ 0.03 mM), a bilayer is formed at intermediate concentrations (0.03 $<$ [CTAB] $<$ 1 mM), and bilayer-type aggregates are formed at concentrations near the critical micelle concentration ([CTAB] $>$ 1 mM). Meena and Sulpizi[28] and da Silva *et al.*[29] separately carried out simulations on planar gold interfaces capped with CTAB and found that the CTAB molecules form cylindrical micelles near the gold surface. Simulation studies of CTAB-capped spherical nanoparticles by Kalipillai *et al.* showed that at a concentration of 0.25 M, the CTAB forms a monolayer rather than a bilayer at the gold surface, and immobilization of bromide ions induces the formation of micelle aggregates.[30] These studies were important steps in understanding

the structural features of CTAB at the surface of gold nanoparticles, but there is no consensus yet on whether CTAB forms bilayer or monolayer structures.

Simulations of heat transfer through gold interfaces have been of recent interest. A variety of factors have been attributed to the conductance through gold-water interfaces, including interfacial wettability,[31] the choice of water model and boundary conditions,[31] spectral overlap in the vibrationald densities of state (VDOS) of gold and water,[32] and the presence of water molecules acting as energy carriers at the gold surface.[33–35] However, when the gold is functionalized, other factors can influence the conductance. A study by Wu *et al.* found that in systems containing functionalized gold nanorods, the conductance was higher when the gold was functionalized with polyethylene glycol (PEG) rather than CTAB. This difference was attributed to the hydrophobic nature of CTAB and its lack of strong interactions with both the gold and water solvent.[36] Therefore, continued studies of the effects of gold functionalization on heat transfer processes are needed.

In the sections that follow, we outline non-equilibrium molecular dynamics simulations of thermal transport through gold interfaces that have been functionalized with CTAB or MTAB and solvated in water. These simulations encompass both planar gold interfaces as well as small nanoparticles in non-periodic geometries. We are utilizing velocity shearing and scaling reverse non-equilibrium molecular dynamics (VSS-RNEMD) to create a thermal flux between the aqueous regions and the metal, and the system responds with thermal gradients in bulk regions and a temperature drop across the interface. This allows for calculation of both bulk thermal conductivity and the interfacial thermal conductance in planar[37] and spherical[38] geometries.

Computational Details

Force Fields

The unified atom force field parameters for CTAB and MTAB (see Fig. 1) were adapted from multiple sources. For most of the sites in the ligands, the Lennard-Jones, bond, bend, and torsion parameters were taken from Ríos-López *et al.*[39] TraPPE-UA force field parameters were used

to describe interactions involving the sulfur and adjacent carbon atoms,[40] with bond and stretch constants adapted from previous work using both TraPPE- and OPLS-derived force fields.[41–44] Interactions between gold and the other atoms were taken from Schapotschnikow *et al.* and Pool *et al.*[45,46]

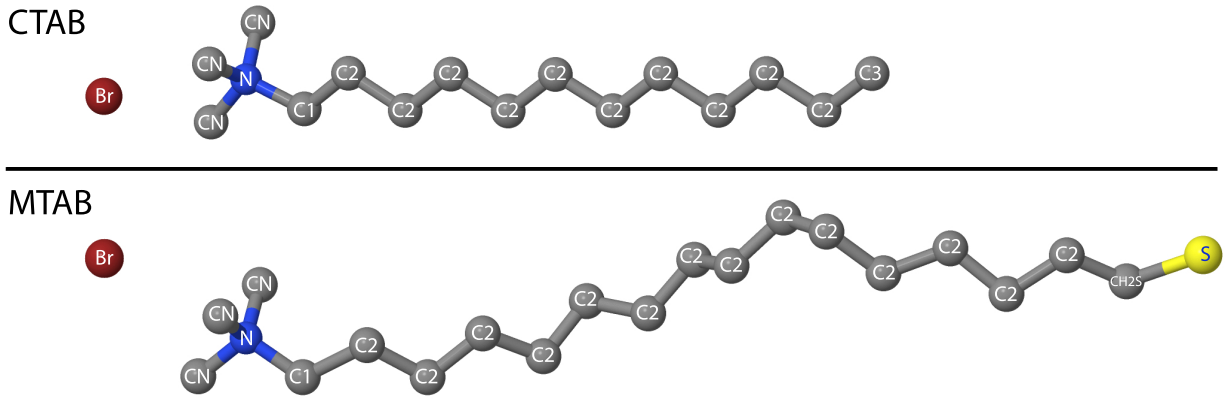

Figure 1: The unified atom (UA) ligand salts used in this study. CTAB (cetyltrimethylammonium bromide) is hypothesized to form bilayers on the surface of gold nanostructures, while the sulfur atom in MTAB (16-mercapto-hexadecyl-trimethylammonium bromide) binds directly to the metal, creating a monolayer on the surface with the polar / ionic ends of the molecule free in the aqueous solution. Force field parameters for all atom types are provided in the Supporting Information (SI).

We have utilized the density-readjusted embedded atom method (DR-EAM)[47] which has previously been shown to affect the interfacial thermal conductance through pristine[48] and citrate-capped[49,50] gold interfaces. The effects of including metal polarizability are compared to systems simulated using the non-polarizable embedded atom method (EAM) as parameterized by Zhou, Johnson, and Wadley.[51]

Rigid SPC/E water was used as the solvent in all systems.[52] The gold-water interactions were modified from work by Dou *et al.*[53] All of the parameters utilized in this work are provided in the Supporting Information (SI).

Simulation Protocol

A series of planar and spherical gold structures were modeled in this work: Planar structures which exposed the (111), (110), and (100) facets to the ligands and solvent, as well as spherical nanoparticles with a 10 Å radius. Three different surface treatments were studied on these gold structures, including CTAB with an approximate packing density of 3.35 molecules per nm^2, MTAB with the same packing density, and MTAB with a density of approximately 1.65 molecules per nm^2. The lower MTAB packing density approximates the monolayer coverage of CTAB in the Kawasaki, Nishimura, and Arakawa experiments.[27] The higher surface concentration of MTAB (and CTAB) was taken from the same study, in which the critical micelle concentration of CTAB was determined to be 3.35 CTAB molecules per nm^2.[27] Each of these systems were simulated using both the non-polarizable EAM model and the polarizable DR-EAM model.

The planar gold facets were built using slabBuilder, an OpenMD utility, with a lattice constant of 4.08 Å.[54] Packmol was used to generate randomized initial configurations of the ligands.[55] For CTAB, the bromide counter-ions adjacent to the inner CTAB layer were placed approximately 5 Å away from the gold surface. To restrain the initial orientation of the CTAB molecules, the nitrogen and terminal methyl group within each leaf were placed at least 13 Å apart. The terminal methyl groups corresponding to the inner and outer leaves of CTAB molecules were placed at least 6 Å apart. Spherical gold nanoparticles capped with CTAB were simulated, but during equilibration in all replicas, the CTAB formed a bilayer micelle which excluded the nanoparticles, preventing calculation of interfacial thermal conductance (G). Sample configurations are shown in Figures 2 and 3.

In all cases, five (5) replicas of each simulation were performed, using a random resampling of molecular placements to sample surface attachment of ligands, and random re-seeding of atomic velocities prior to the first equilibration stage. In the sections that follow, all figures and data presented in tables represent the mean of the five replicas and 95% confidence intervals around these means were arrived at using $\varepsilon = 1.96\sigma/\sqrt{N-1}$ where N is the number of replicas, and σ is the standard deviation of the sample mean.

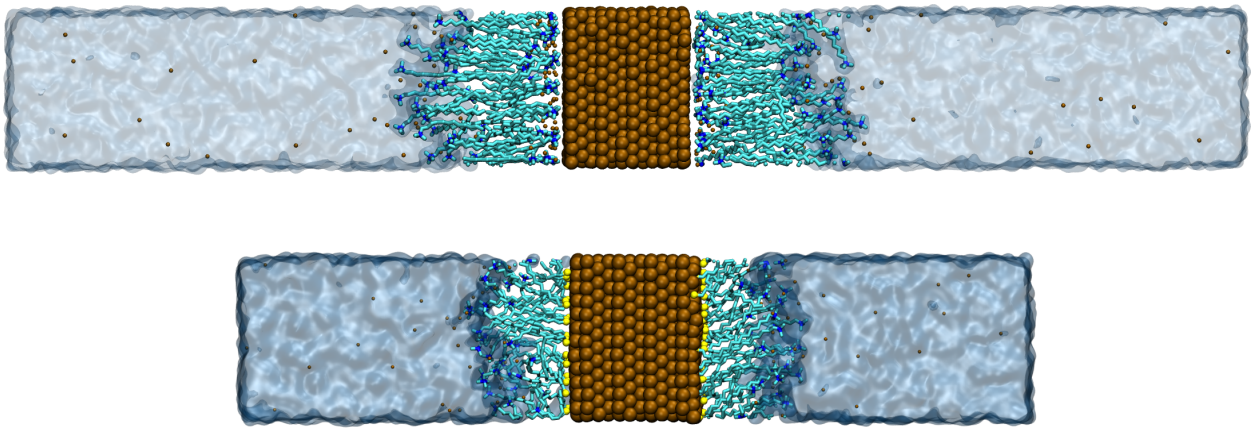

Figure 2: Snapshots of equilibrated (111) planar facets capped with CTAB (top) and high density MTAB (bottom). The low density MTAB systems were constructed identically to the high density systems, but with fewer MTAB molecules. Gold, sulfur, and bromine atoms are represented with van der Waals spheres, while the rest of the ligands are shown with bonds. The water solvent is shown as translucent.

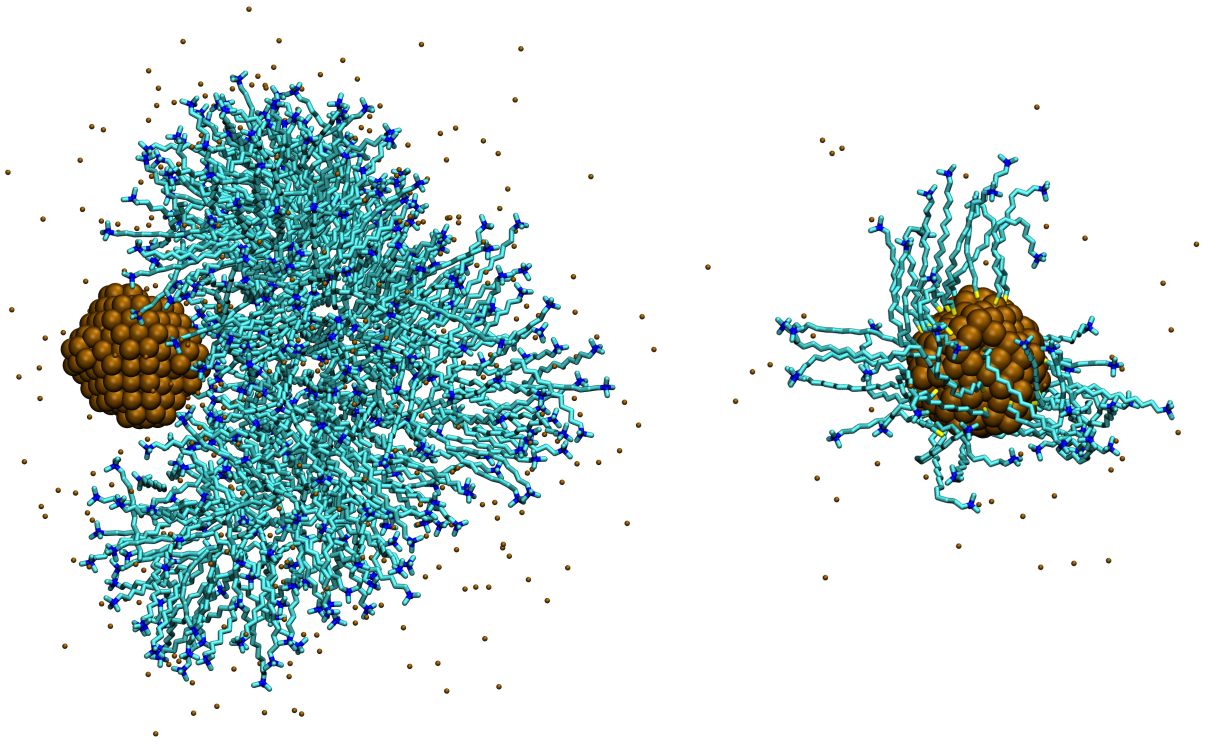

Figure 3: Snapshots of spherical nanoparticles capped with both CTAB (left) and with high density MTAB (right). While both systems stayed intact through the equilibration process, the gold was ejected from the CTAB micelle during the application of the thermal flux. This phenomenon occurred with all simulation replicas, but did not occur for any of the MTAB simulations. Water has been omitted for visual clarity.

The planar gold facets capped with MTAB were built using a similar protocol to the one described above.[54,55] The sulfur atoms in MTAB were placed approximately 5 Å away from the gold surface. The amine nitrogen was placed at least 20 Å away from the carbon proximal to sulfur to force the MTAB molecules into roughly linear starting configurations.

Initial configurations were relaxed using steepest descent minimization of the configurational energy. Before equilibration, the atoms in each system were given velocities that were sampled from a Maxwell-Boltzmann distribution at 300 K. All systems with polarizable gold atoms were briefly simulated for 1 ps with a time step of 0.2 fs to allow equilibration of the charge degrees of freedom.

The equilibration protocol for the planar systems is as follows: First, the systems were simulated for 100 ps in the canonical (NVT) ensemble, followed by 1 ns in the isobaric-isothermal (NPT) ensemble with separate barostats for each dimension to allow the box lengths in each dimension to adjust separately. Characteristic time constants for the barostat and thermostat extended system variables were set to 5 ps and 100 fs, respectively. The systems were then simulated for 0.5 ns in the NVT ensemble, followed by 0.5 ns in the microcanonical (NVE) ensemble. A time step of 1 fs was used for all equilibration and data collection simulations.

Spherical systems were built with a radius of 10 Å and a lattice constant of 4.08 Å using nanoparticleBuilder, another OpenMD utility.[54] The bare gold nanosphere was first equilibrated by assigning atomic velocities sampled from a Boltzmann distribution at 5 K and simulating using the non-periodic Langevin Hull integratorfor 200 ps.[56] This process was repeated while increasing the temperatures to 100, 200, and finally 300 K. Packmol[55] and OpenMD[54] were used to combine the gold with the ligand and solvent components, and the gold atom closest to the center of the nanoparticle was given an artificially large mass to prevent the nanoparticle from drifting during simulations. The MTAB sulfur atom on each ligand was placed within 4 Å of the gold surface, and the position of one of the central CH_2 groups was required to be at least 11 Å away. Snapshots of spherical systems capped with MTAB are shown in Figure 3.

The combined spherical systems were first simulated for 200 ps using the Langevin Hull inte-

grator during which the atomic velocities were resampled from a Maxwell Boltzmann distribution at 300 K every ps. The spheres were then simulated for an additional 250 ps without velocity resampling.

After equilibration, a thermal flux was applied to all systems using the VSS-RNEMD methodology.[37,38] In most cases, the flux was chosen so the heat rate at the interface between the metal and solvent was roughly equal, but the magnitude had to be adjusted for some systems to produce a temperature difference that was large enough to be measurable. The applied flux was 2.0×10^{-6} kcal mol^{-1}Å^{-2} fs^{-1} (1400 MW m^{-2}) or 2.5×10^{-6} kcal mol^{-1}Å^{-2} fs^{-1} (1800 MW m^{-2}) for the planar systems and 6.0×10^{-6} kcal mol^{-1}Å^{-2} fs^{-1} (4300 MW m^{-2}) for the MTAB-capped nanospheres. The thermal flux was applied for 5 ns in the planar systems and 3.5 ns in the nanospheres. All subsequent data collected from these simulations was from the entirety of the 5 ns RNEMD simulation for planar systems, but only the last ns was used for the nanospheres.

We note that the RNEMD algorithm being utilized (VSS-RNEMD) applies a thermal flux and does not have fixed source and sink temperatures. However, these values of applied thermal flux allowed the systems to come to steady-state interfacial temperature differences within the equilibration period, with ΔT values in the range of $\sim 50-65$ K for the planar CTAB systems, $\sim 10-15$ K for the planar MTAB systems, and $\sim$ 5K for the nanoparticle systems. VSS-RNEMD also samples from configurations with fixed total energies and contributes only a very small energy drift during the simulations. We observe a typical energy drift of < 0.8kcal mol^{-1} ns^{-1}. In general, the RNEMD method is a smaller contribution to energy drift than the use of polarizable metal potentials.

Results

Thermal Transport Properties

Fourier's law,

$$\mathbf{J} = -\lambda \nabla T, \tag{1}$$

was used to calculate the solvent thermal conductivity (λ) where $\mathbf{J}$ is the (applied) thermal flux and ∇T is the temperature gradient. In planar systems, λ is calculated by measuring ∇T in the region where only solvent exists. In these systems, the bromide counter-ion is present as well. The interfacial thermal conductance,

$$G = \left(\frac{J_z}{\Delta T} \right) \tag{2}$$

is used to understand the rate at which heat passes through the interface between solid and liquid phases. Here, ΔT is the temperature difference across the interface. In planar systems, ΔT is measured from a location that contains only gold to a location that contains only solvent, and the interface spans the entire distance occupied by the capping agents. In spherical systems, we utilize a series approximation for the interfacial thermal resistance

$$R_K = \frac{1}{G} = \frac{1}{q_r} \sum_i 4\pi r_i^2 \left(T(r_{i+1}) - T(r_i) \right) \tag{3}$$

where q_r is the radial heat rate, and spherical shell i has a radius r_i with temperature $T(r_i)$. For this measurement, the systems are divided into concentric spherical shells, where heat passes from one shell to the next. The interface is defined identically here as in the planar systems, as it begins at a location that contains only gold and ends at a location that contains only water.

The solvent thermal conductivity and interfacial thermal conductance values for the planar CTAB and MTAB systems were calculated and are shown in Table 1. Solvent thermal conductivities (λ) are higher than those experimentally observed for water (~ 0.6 Wm^{-1} K^{-1}). This is likely due to the presence of bromide ions in the solution, although we note that the solution phase thermal conductivities are in reasonable agreement with those for neat SPC/E that were obtained by Bresme's group ($\lambda = 0.87 \pm 0.04$ Wm^{-1} K^{-1}).[57,58] They are also in agreement with the solution phase values ($\lambda = 1.0 \pm 0.03$ Wm^{-1} K^{-1}) we obtained in a study of metal nanostructures in a 0.12M sodium citrate solution.[49,50] The interfacial conductance is much lower in systems contain-

ing CTAB than in those containing MTAB. When the packing density of MTAB is changed, we observe some small differences in G. Interestingly, polarizability of the metal leads to an increase in G only in the systems that contain CTAB, and there are small differences in G between the planar facets in these systems.

Table 1: Solvent thermal conductivity (λ) in $\mathbf{Wm^{-1}\,K^{-1}}$ and interfacial thermal conductance (G) in $\mathbf{MW\,m^{-2}\,K^{-1}}$ for planar gold interfaces capped with CTAB and MTAB ligands. Where uncertainties are in the last digit, they are indicated in parentheses.

Solution Phase	Metal Structure	Non-polarizable		Polarizable	
		λ	G	λ	G
3.35 CTAB / nm^2	planar (111)	0.93(3)	20.8(3)	0.95(3)	25.2(4)
	planar (110)	0.91(4)	19.8(3)	0.91(4)	23.7(7)
	planar (100)	0.90(4)	18.5(3)	0.89(3)	21.5(3)
3.35 MTAB / nm^2	planar (111)	0.91(4)	125(4)	0.92(4)	133(3)
	planar (110)	0.88(4)	127(7)	0.92(3)	129(5)
	planar (100)	0.89(3)	125(3)	0.89(3)	123(6)
	sphere, $r = 10$ Å	–	125 ± 23	–	112 ± 21
1.65 MTAB / nm^2	planar (111)	0.82(3)	136(6)	0.82(4)	143(6)
	planar (110)	0.85(2)	136(2)	0.84(3)	140(3)
	planar (100)	0.84(3)	128(5)	0.87(4)	127(5)
	sphere, $r = 10$ Å	–	121 ± 23	–	173 ± 102

The conductance values for the MTAB-capped nanospheres were also computed and are shown in Table 1. Spatial clustering of the MTAB ligands into dense patches on the spherical nanoparticles yields significant uncertainty in the value of the interfacial conductance in these systems, and we note that the planar conductance falls within these error estimates (for the same coverage). When we consider only the systems containing MTAB, G does not appear to depend strongly on surface curvature or on the treatment of polarizability. This has been previously observed in gold interfaces capped with a low molecular weight thiolated polyethylene glycol (PEG).[50,59] In cases

where there is strong metal-to-ligand coupling provided by the S-Au bond, G is dominated by this coupling over other factors. As a comparison with the MTAB data in Table 1, thiolated PEG ligands exhibit interfacial thermal conductance ($G \sim 210$ MWm^{-2}K^{-1}),[59] significantly higher than either the CTAB or MTAB interfaces. These findings support the conclusions in simulations of gold nanorods by Wu *et al.*[36] which determined that conductance is higher in PEG- rather than CTAB-functionalized gold interfaces. In both MTAB and thiolated PEG, the metal-to-ligand bonding is identical, so this change in behavior arises from the ability of thiolated PEG to form hydrogen bonds with the surrounding water. MTAB interacts with the solvent primarily through charge-dipole interactions at the trimethylammonium head group, and the bulky head group also prevents interpenetration of the solvent layer close to the surface.

To help explain these trends in conductance and explore the surface environments of each system, we have computed a number of measures of the interactions between the various species. We first discuss the thermal profiles and the local mass densities of all species relative to the interface. We have also investigated the role of orientational ordering in the MTAB layers, the overlap in the vibrational densities of states, the physical contact between ligand and solvent species, and the charge penetration in the polarizable metal surface. These are described in detail in the remainder of this section.

Interpenetration of Ligand and Solvent Layers

We show the local mass densities of all species and their corresponding thermal profiles in Figures 4 –6. Similar figures for the polarizable systems are shown in the SI in Figures S2 – S4. We observed a large temperature drop (ΔT) across the interface in the CTAB systems (Figures 4 and S2), indicating that CTAB is relatively poor at conducting heat to the solvent. CTAB's bilayer structure contains bulky head groups, impeding solvent diffusion to the surface, so very little solvent is present near the gold surface. We also observe some differences in the clustering of bromide counter-ions near the gold surface.

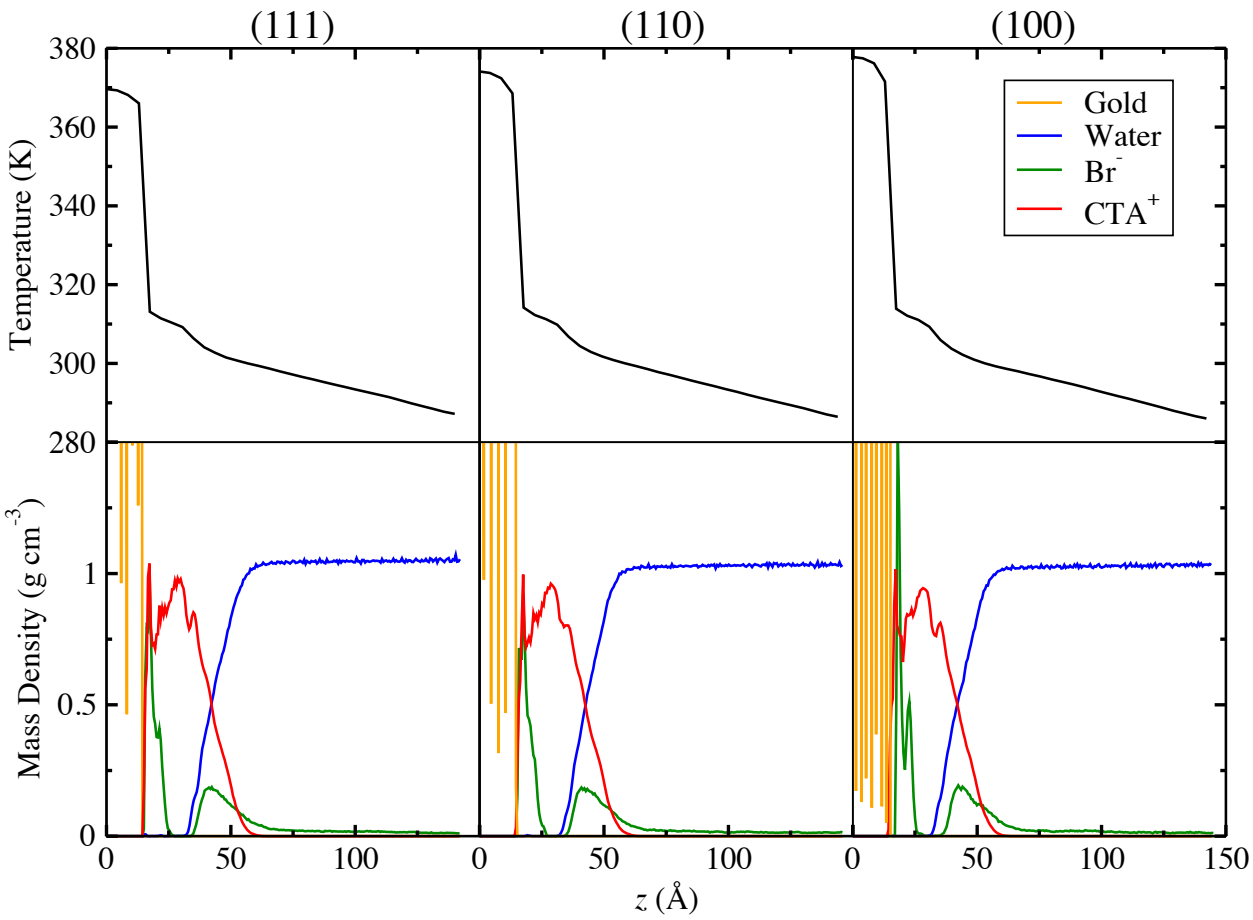

Figure 4: Temperature (top) and mass density (bottom) profiles in systems with non-polarizable planar gold interfaces capped with CTAB. Only a small number of water molecules are present among the CTA^+ ligands and solvent is generally impeded from reaching the gold surface by the bulky head groups. Two peaks representing bromide counter ions are consistent with the location of the CTA^+ head groups.

In the planar MTAB systems we observe a much smaller temperature drop for the same imposed kinetic energy flux, indicating that this ligand provides higher thermal conductance to the solvent. In the lower density MTAB layers, water can easily diffuse into the ligand layer and clusters near the interface. With a higher ligand packing density, fewer water molecules are able to cluster near the interface. Previous simulations of thiolated ligands on gold have observed surface reconstruction as sulfur atoms bury into the outer planar layer at the surface.[50,59] In the MTAB density profiles, the bulky TAB^+ head groups appear to be preventing this surface behavior. Consistent with the results in Table 1, there are no notable differences in the local mass densities when

the metal is treated as a polarizable medium (Figures S3 and S4 in the SI).

In the nanospheres, the TAB^+ head groups are not packed tightly, allowing for more conformational freedom of the chains, and the sulfur atom of MTAB can then penetrate into the gold surfaces. The gold surfaces are deformed significantly from their initial spherical structures, and a small fraction of water molecules also cluster near the surface (some within the original 10 Å particle radius). This disruption of the gold surface, burial of the sulfur, and surface water clustering is observed whether or not the treatment of the metal is polarizable.

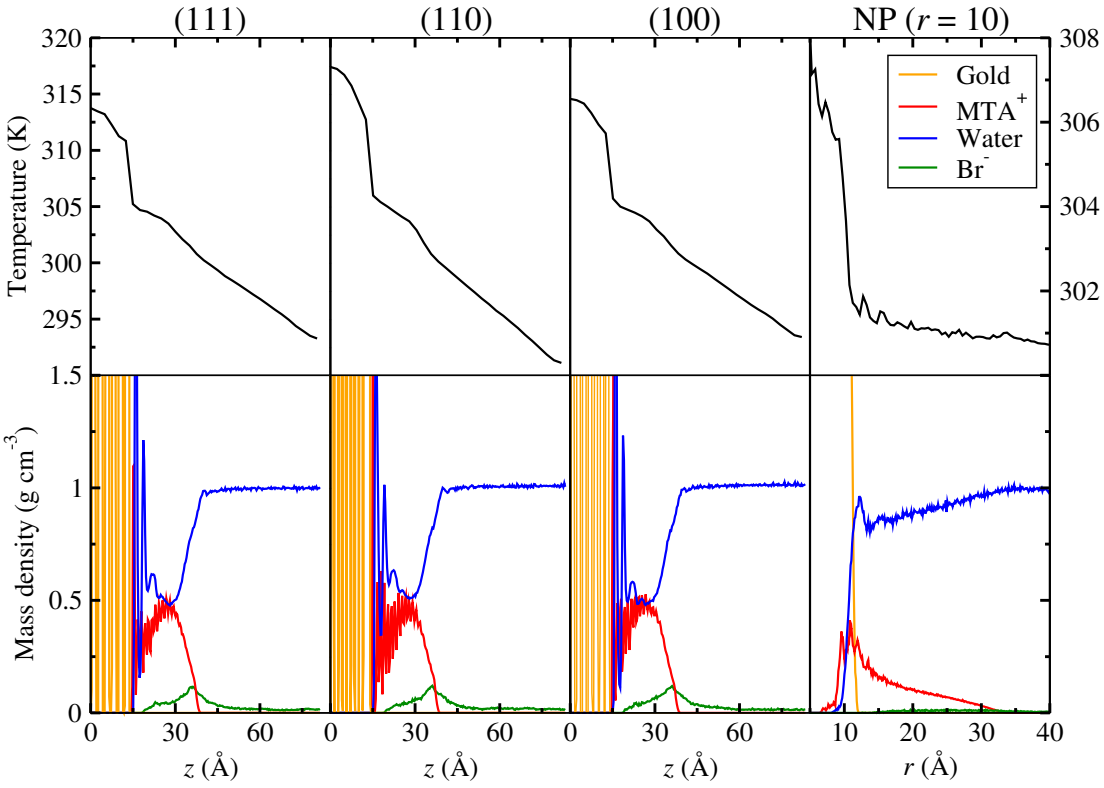

Figure 5: Temperature (top) and mass density (bottom) profiles in systems with non-polarizable planar gold interfaces capped with MTAB, highlighting the region directly adjacent to the surface. Here the MTAB packing density is 1.65 molecules/nm^2. Water can be found adjacent to the gold surface, as the lower density of MTAB ligands provide more space for water molecules to diffuse into the ligand layer. The bromide counter ions are much more diffuse here than in the CTAB systems, and the Br^- density is greatest near the location of the MTA^+ head groups.

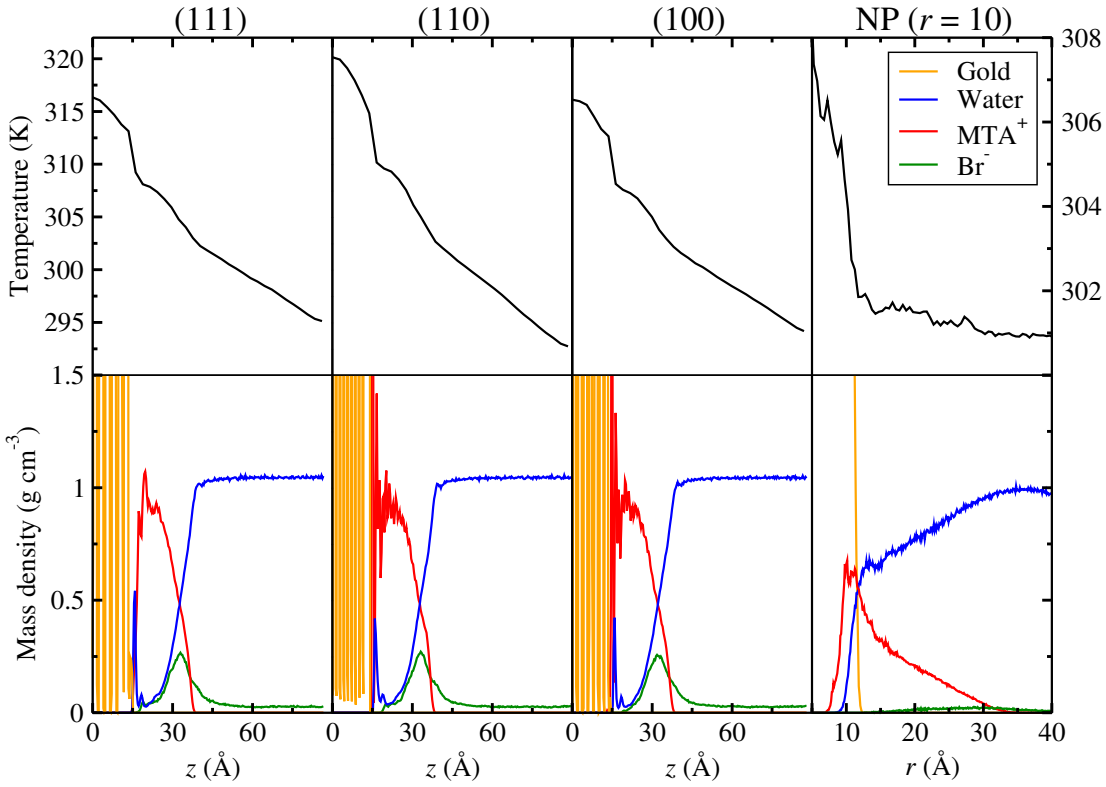

Figure 6: Temperature (top) and mass density (bottom) profiles in systems with non-polarizable planar gold interfaces capped with MTAB, highlighting the region directly adjacent to the surface. Here the MTAB packing density is 3.35 molecules/nm^2.

In all of these systems, the drop in temperature is most significant between the gold surface and the ligand layer, with an additional drop in temperature between the ligand layer and the solvent. While ballistic transport has been observed at molecular junctions,[60] the transport through the CTAB and MTAB layers appears to follow Fourier's law. In the sections that follow we discuss orientational ordering and solvent interpenetration of the ligand layers, hinting at ligand-phase disorder, which could potentially explain non-ballistic transport.

Orientational Ordering of Ligand Layers

A measure of the orientational ordering of the MTAB ligand layer is provided by the second order Legendre parameter,

$$\langle P_2 \rangle = \frac{1}{2} \left\langle 3\cos^2\theta - 1 \right\rangle \tag{4}$$

where θ is the angle formed between the particular molecule and the director axis for all MTAB molecules. A similar order parameter measuring orientational ordering perpendicular to the surface normal can be defined,

$$\left\langle P_2^{\perp} \right\rangle = \frac{1}{2} \left\langle 3\ (\hat{\mathbf{u}}_i \cdot \hat{\mathbf{n}}_i)^2 - 1 \right\rangle \tag{5}$$

where $\hat{\mathbf{u}}_i$ is the unit vector pointing along the long axis of molecule i and $\hat{\mathbf{n}}_i$ is the unit surface normal at that molecule's attachment point. For planar interfaces, $\hat{\mathbf{n}}_i = \hat{\mathbf{z}}$, but for the nanospheres, $\hat{\mathbf{n}}_i = \hat{\mathbf{r}}_i$. In all cases, $\hat{\mathbf{u}}_i$ is the unit vector between the the sulfur and nitrogen atoms in MTAB. Complete orientational disorder would yield a $\langle P_2 \rangle$ value of 0. If $\left\langle P_2^{\perp} \right\rangle = 1$, this would indicate that all ligands are oriented normal to the gold surface, while complete orientational alignment between MTAB ligands would yield a $\langle P_2 \rangle$ of 1. The computed $\langle P_2 \rangle$ and $\left\langle P_2^{\perp} \right\rangle$ values are shown in Table 2.

Table 2: Orientational Order Parameters Between Sulfur and Nitrogen in MTAB

Solution Phase	Metal Structure	Non-polarizable		Polarizable	
		$\langle P_2 \rangle$	$\left\langle P_2^{\perp} \right\rangle$	$\langle P_2 \rangle$	$\left\langle P_2^{\perp} \right\rangle$
3.35 MTAB / nm^2	planar (111)	0.52(9)	0.44(6)	0.52(3)	0.42(4)
	planar (110)	0.56(3)	0.49(2)	0.58(3)	0.50(5)
	planar (100)	0.57(5)	0.49(4)	0.60(7)	0.49(4)
	sphere, $r = 10$ Å	–	0.64(6)	–	0.60(7)
1.65 MTAB / nm^2	planar (111)	0.63(4)	0.57(6)	0.61(5)	0.59(4)
	planar (110)	0.64(3)	0.63(3)	0.64(4)	0.61(5)
	planar (100)	0.60(6)	0.58(6)	0.54(6)	0.51(6)
	sphere, $r = 10$ Å	–	0.73(6)	–	0.69(6)

The general picture that develops for planar systems is that the higher density MTAB layers are orientationally ordered, but that the molecules must be tilted relative to the surface normal, as the $\langle P_2 \rangle$ and $\langle P_2^{\perp} \rangle$ parameters show significant differences. This can only happen if the molecular director axis is not aligned with the surface normal, which can be seen in Figure 7. In the lower density MTAB layers, both orientational order parameters are almost identical, indicating that the director axis for these molecules is perpendicular to the surface. For the spherical nanoparticles, the surface-attached ligands have no director axis (in the sense of liquid crystalline molecules), but the surface normal $\langle P_2^{\perp} \rangle$ indicates a similar degree of orientational ordering as $\langle P_2 \rangle$ for the planar systems.

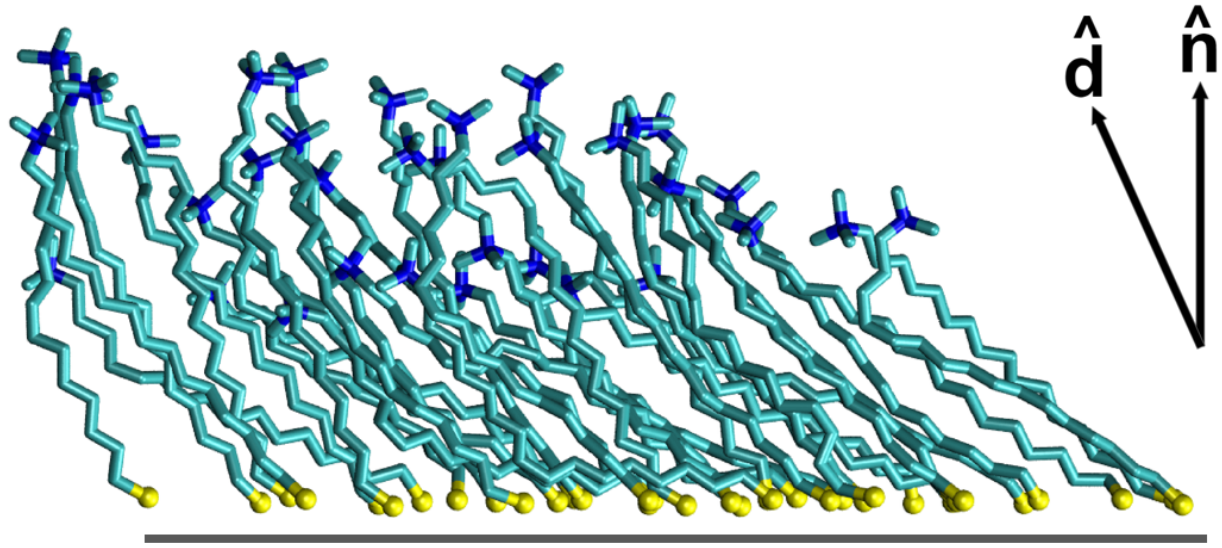

Figure 7: Snapshot of an MTAB ligand layer with a packing density of 3.35 molecules/nm^2. The gray line represents the gold surface. The director axis, $\hat{\mathbf{d}}$, is the average orientation of adsorbed ligands, and at this MTAB coverage, $\hat{\mathbf{d}}$ is tilted by 24.5° relative to the surface normal ($\hat{\mathbf{n}}$).

Overlap in Vibrational Densities of State

The diffuse mismatch model (DMM) is sometimes used to understand heat transfer at interfaces.[61] In DMM, the interfacial thermal conductance between materials a and b

$$G_{ab} = \frac{1}{4\pi} \sum_p \int_0^{\pi/2} \sin\theta d\theta \int_0^{2\pi} d\phi \int_0^{\infty} d\omega \left(\hbar\omega \frac{\partial f}{\partial T} \nu_a \rho_a(\omega) \tau_{ab} \cos\theta \right) \tag{6}$$

where f is the Bose-Einstein function

$$f(\omega,T) = \frac{1}{(e^{\hbar\omega/k_BT}-1)}, \tag{7}$$

and phonons with a polarization p, group velocity $v_a(\omega,p)$, and incident angles θ and ϕ are transmitted between a and b with a transmission probability $\tau_{ab}(\omega)$.[62] The Bose-Einstein function weights the lower frequency portion of the vibrational spectra, where heat carrying modes are present. To connect forward and reverse scattering at some frequency ω, we can use detailed balance, where $\tau_{ab}(\omega) = 1-\tau_{ba}(\omega)$. The frequency-dependent portion of Eq. (6) can be treated in a symmetric form, where

$$\rho_a(\omega)\tau_{ab}(\omega) \approx \frac{\rho_a(\omega)\rho_b(\omega)}{\rho_a(\omega)+\rho_b(\omega)}. \tag{8}$$

We note that the DMM is not quantitative and does not accurately predict the magnitude of heat transfer between adjacent materials, but we can qualitatively examine the model to attempt to understand whether vibrational acoustic mismatch is important for efficient heat transfer at these interfaces. To examine the vibrational mismatch, we have computed the power spectra for vibrational motion projected in a direction normal to the interface,

$$\rho_\perp(\omega) = \frac{1}{\sqrt{2\pi}}\int_{-\infty}^{\infty}\langle v_\perp(t)\cdot v_\perp(0)\rangle e^{-i\omega t}\,dt \tag{9}$$

where the angle bracket averages over all particles j, and the perpendicular velocities for those particles,

$$v_{j,\perp}(t) = \mathbf{v}_j(t)\cdot\hat{\mathbf{n}}(\mathbf{r}_j) \tag{10}$$

and $\hat{\mathbf{n}}(\mathbf{r}_j)$ is the unit vector normal to the interface at the location ($\mathbf{r}_j$) of atom j. In planar systems, the normal direction is the z axis, but for nanoparticles, the radial vector from the particle center determines the normal direction. Using velocity projections perpendicular to the interface has the effect of integrating over incoming phonon scattering angle and phonon polarization in Eq. (6).

We divided the systems into three regions: gold atoms, ligand molecules, and interfacial sol-

vent (trapped in the ligand layer, or within 5 Å of the terminal TAB^+), for both the planar and nanoparticle systems. Each system was simulated for an additional 50 ps in the NVE ensemble for the planar systems and the Langevin Hull (NPT) for the nanoparticle systems. Velocity autocorrelation functions with a time granularity of 3 fs were calculated from these trajectories. The power spectra are discrete Fourier transforms of these autocorrelation functions.

The low-frequency portion (up to 250 cm^{-1}) of the vibrational power spectra for each species in non-polarizable (111) facets containing CTAB and high density MTAB are shown in Figure 8. There is overlap between the gold and ligand in both systems, although the two of the ligand spectra differ greatly in this region. The CTAB spectrum contains distinct peaks at approximately 25 and 100 cm^{-1}, while the MTAB spectrum is relatively unstructured. While there is a peak in both ligand spectra at approximately 180 cm^{-1}, it is larger and more distinct for CTAB. The gold and interfacial solvent spectra are generally indistinguishable between the two systems. Versions of this data covering the full frequency range are provided in the SI as Figure S5.

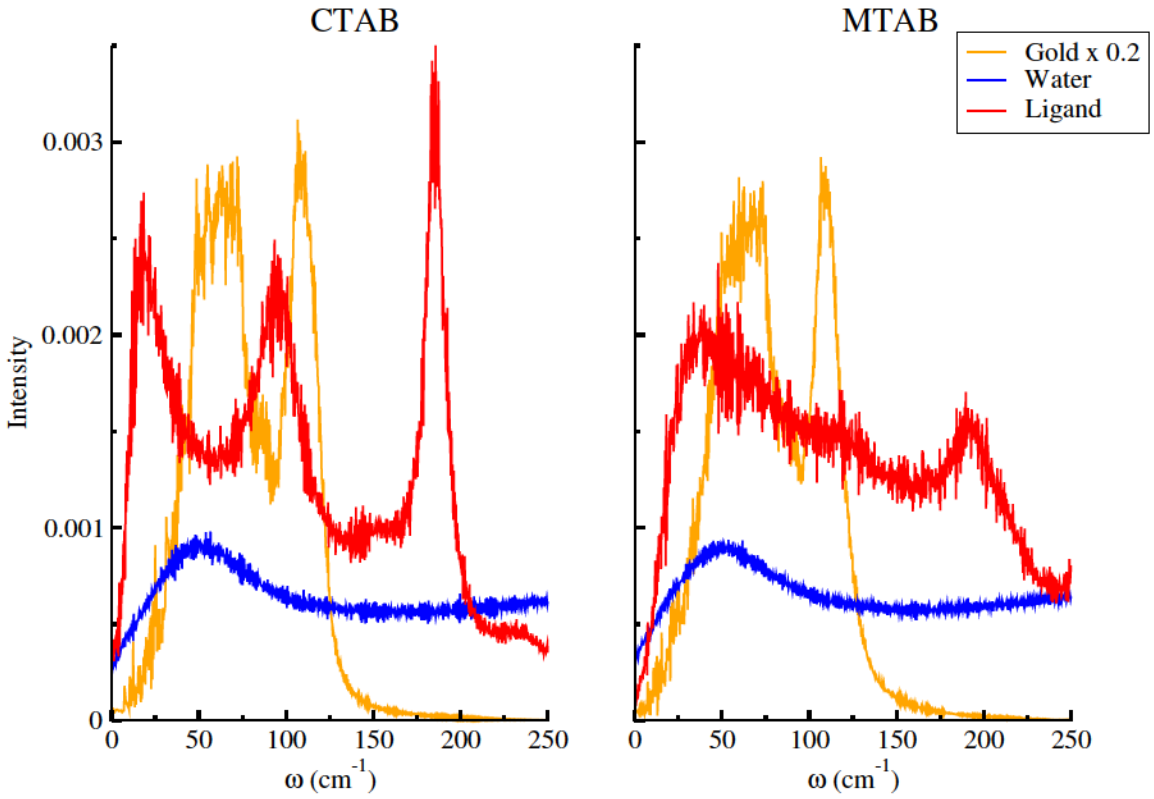

Figure 8: Vibrational densities of states (VDOS) for all species in non-polarizable (111) facets containing either CTAB or the high density MTAB. The low frequency ($0 - 250\ \mathrm{cm}^{-1}$) are shown here. While there are differences in the ligand spectra, spectral overlap (Eq. (11)) is not significantly different for these ligands with either their corresponding gold spectra, or the interfacial solvent.

The vibrational densities of states of all species in spherical MTAB systems, at both low and high densities, are shown in Figure 9, highlighting the low frequency ($0 - 250\ \mathrm{cm}^{-1}$) heat-carrying modes. As is the case in the planar systems, only interfacial solvent is shown. In the low density MTAB systems, the gold peak around $70\ \mathrm{cm}^{-1}$ is a bit larger in magnitude than in the high density systems. Regardless of the MTAB density, the ligand spectra do not differ significantly, and the solvent spectra are also unchanged. There are no obvious differences in the spectra of any species in non-polarizable versus polarizable systems. All VDOS results for the polarizable systems are provided in the SI.

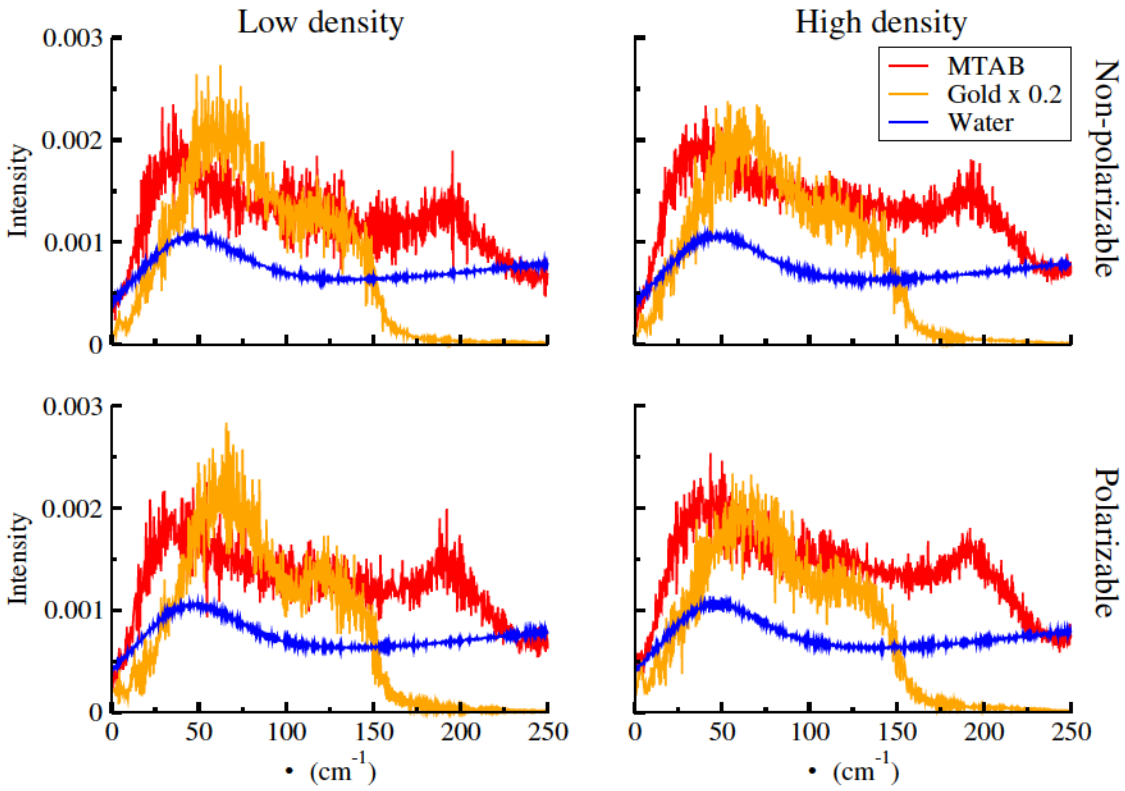

Figure 9: Vibrational densities of states (VDOS) for all species for high and low density spherical MTAB systems. Other than small differences around 70 cm^{-1} in the gold spectra between high and low density systems, there are no significant differences in the other species.

A vibrational overlap parameter,

$$O_{ab} = \int_0^\infty d\omega\, \hbar\omega \left(\frac{\partial f}{\partial T}\right) \frac{\rho_a(\omega)\rho_b(\omega)}{\rho_a(\omega)+\rho_b(\omega)}\,, \tag{11}$$

represents the frequency-weighted overlap portion of the DMM expression for G. Here, $\rho_a(\omega)$ and $\rho_b(\omega)$ are normalized densities of states for the two species, and the derivative of the Bose-Einstein function effectively weights the lowest frequency portion of the spectra (0–150 cm^{-1}). The densities of states are defined in Eq. (9), with velocities projected in a direction perpendicular to the interface. Data on the overlap values are provided in Table 3.

The overlap in power spectra between species, as defined by Eq. (11), is not predictive of the differences in interfacial thermal conductance. While there are notable differences in the structures of the ligand spectra, the integrated overlap between the gold/MTAB and gold/CTAB pairs appear to be roughly equal, despite the significantly higher G values in MTAB systems. Rather, the presence of the strong Au-S bond is a better predictor of increased conductance, and interpenetration by the ligand and solvent also plays a role. This is further evidence that the predictions of DMM are missing important information about the inter-species contact.

Table 3: Vibrational Density of States overlap between ligand/gold and ligand/water pairs

Solution Phase	Metal Structure	Non-polarizable		Polarizable	
		Gold	Water	Gold	Water
3.35 CTAB / nm^2	planar (111)	0.103(1)	0.049(3)	0.102(3)	0.048(1)
	planar (110)	0.104(3)	0.049(1)	0.106(4)	0.049(1)
	planar (100)	0.108(4)	0.050(1)	0.104(2)	0.0488(2)
3.35 MTAB / nm^2	planar (111)	0.109(4)	0.049(1)	0.112(3)	0.049(1)
	planar (110)	0.109(2)	0.049(3)	0.107(3)	0.048(1)
	planar (100)	0.112(4)	0.050(1)	0.112(4)	0.0490(4)
	sphere, $r = 10$ Å	0.113(3)	0.054(1)	0.116(6)	0.055(1)
1.65 MTAB / nm^2	planar (111)	0.101(2)	0.049(1)	0.098(2)	0.047(1)
	planar (110)	0.103(3)	0.048(1)	0.102(4)	0.047(1)
	planar (100)	0.102(6)	0.049(1)	0.102(4)	0.048(1)
	sphere, $r = 10$ Å	0.102(6)	0.052(1)	0.103(4)	0.052(1)

Physical Contact Between Species

In previous studies of gold interfaces functionalized with thiolated ligands in liquid phase solvents, increased contact between the ligand and solvent was correlated with higher conductance through the interface.[50,59,63] To determine if the same trend was present in this work, we calculated the Bhattacharyya coefficients (BC) for both ligand/gold and ligand/solvent pairs using normalized

mass densities. In planar systems containing molecules A and B,

$$BC = \int_{z_L}^{z_R} \sqrt{p_A(z) p_B(z)}\, dz \tag{12}$$

where $p_A(z)$ and $p_B(z)$ are the probability densities of molecules A and B, respectively, calculated using

$$p_A(z) = \frac{\rho_A(z)}{\int_{z_L}^{z_R} \rho_A(z)\, dz} \tag{13}$$

for species A, where $\rho_A(z)$ is the mass density of species A and the bounds of the integrals are the outermost locations of the ligand in the z direction. Similarly, for spherical systems,

$$BC = \int_{r_{\text{inner}}}^{r_{\text{outer}}} 4\pi r^2 \sqrt{p_A(r) p_B(r)} dr \tag{14}$$

where $p_A(r)$ and $p_B(r)$ are the probability densities of molecules A and B, respectively. Likewise, in spherical geometries, the probability densities,

$$p_A(r) = \frac{\rho_A(r)}{\int_{r_{\text{inner}}}^{r_{\text{outer}}} 4\pi r^2 \rho_A(r) dr} \tag{15}$$

for species A, where $\rho_A(r)$ is the mass density for molecule A and the bounds of the integrals span all values r containing the ligand. Pairs of species with no contact will produce a BC value of 0, while complete overlap signifies a BC value of 1. Other investigations of thermal transport at metal/non-metal interfaces have used BCs to compute the overlap of vibrational densities of states near the interface,[33] while here we are using them to estimate physical contact between two species.

Table 4: Bhattacharyya coefficients (Eqs. (12) and (14)) which estimate the degree of density overlap between ligand and solvent. Uncertainties in the last digit are shown in parentheses.

Solution Phase	Metal Structure	Non-Polarizable	Polarizable
3.35 CTAB / nm^2	planar (111)	0.45(1)	0.45(1)
	planar (110)	0.444(6)	0.47(3)
	planar (100)	0.45(1)	0.446(9)
3.35 MTAB / nm^2	planar (111)	0.69(5)	0.67(5)
	planar (110)	0.70(3)	0.73(4)
	planar (100)	0.66(7)	0.67(7)
	sphere, $r = 10$ Å	0.77(1)	0.787(6)
1.65 MTAB / nm^2	planar (111)	0.861(2)	0.863(3)
	planar (110)	0.879(3)	0.880(2)
	planar (100)	0.858(7)	0.850(8)
	sphere, $r = 10$ Å	0.851(8)	0.830(8)

Of all of the measures we have used to quantify the structure and dynamics of the interfacial region, the BC for the ligand–water pairs correlate most strongly with the trends in G in Table 1. The smallest degree of contact between these species are found in the CTAB systems, as water is nearly excluded from the high density CTAB bilayers. A much larger degree of overlap is present in in the MTAB systems. There is also more contact and overlap between water and the low density MTAB than is observed in the high packing density MTAB. This is also consistent with the higher conductance values found in the lower density MTAB systems. The relatively strong correlation between the ligand–solvent BC and the interfacial thermal conductance is evident in Figure 10.

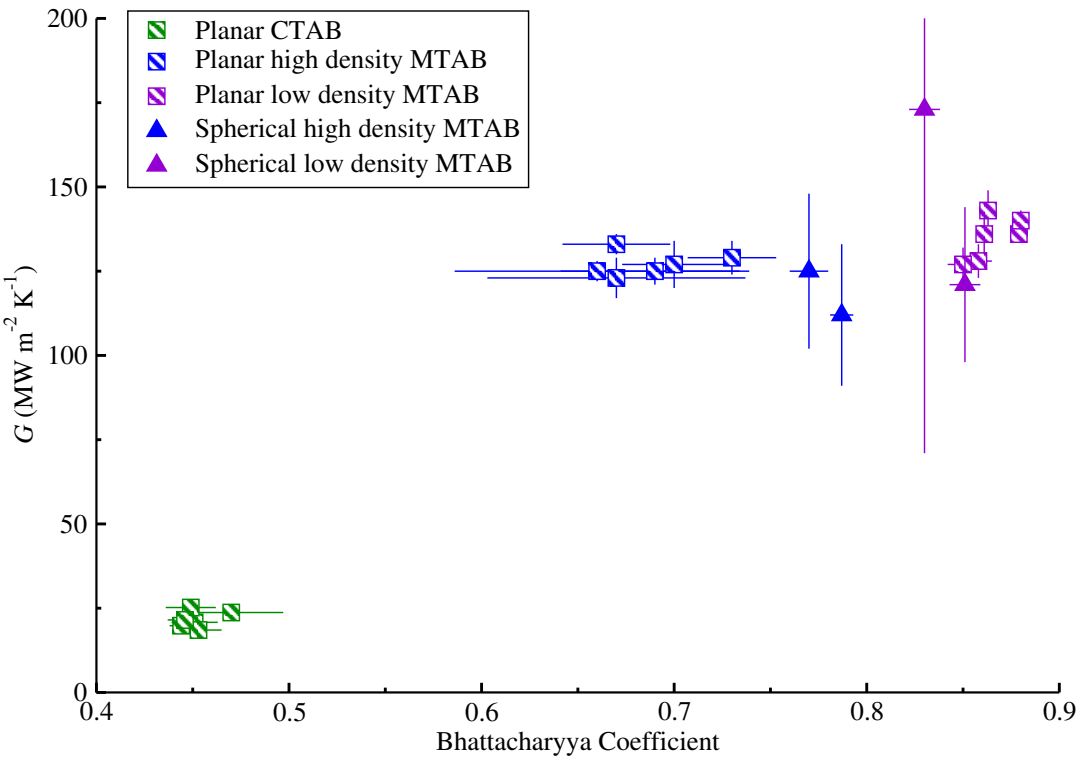

Figure 10: Interfacial thermal conductance correlates strongly with the ligand–solvent density overlap (as measured using Bhattacharyya coefficients). This relationship holds for both the CTAB and MTAB systems.

The BC values for the ligand–gold pairs were also calculated. Given the lack of a strong bond between gold and CTAB, it is no surprise that there is also no density overlap between CTAB and gold in any of the systems. The BC values for the MTAB–gold pair are also $< 10^{-3}$ in the planar systems, which is consistent with the lack of overlap between the mass densities in Figures 5 and 6. However, the BC for the MTAB–gold pair in spherical systems is significantly higher. For the high density MTAB systems, BC = 0.28(3) for non-polarizable systems and 0.26(5) for polarizable systems. For the low density MTAB systems, BC = 0.25(2) for non-polarizable systems and 0.25(4) for polarizable systems. This may simply be an indication of restructuring and faceting of the spherical metal particles, as facets will allow gold atoms on a ridge and adsorbed sulfur atoms on a

flat facet and to have the same radial distance from the center of the particle. We note that this data excludes simulations containing ligands which detached from the metal surface, as this interferes with the normalization of the ligand state density.

We note that in previous studies involving thiolated PEG ligands, BC values from 0.5–0.7 for ligand-water interactions were observed, but these systems also exhibited significant density overlap between the gold and ligand layers (0.05–0.3).[50,59] Both density overlap values provide information about the inter-layer couplings, although no quantitative model has been established between these coefficients and the interfacial thermal conductance.

Examination of Charge Penetration at the Interface

DR-EAM is a polarizable model that uses point charges to represent electronic densities of metallic atoms.[47] Using this model, it is possible to query the degree of charge penetration at the interface. This seems particularly important for CTAB, as the binding motif on gold is thought to be with either the Br^- or TAB^+ moieties in direct contact with the gold surface. The proximity of these ions should create image charges or image dipoles in the metal, altering the coupling between the ligand and the surface. The MTAB systems provide a useful comparison for both the magnitude and depth of polarization in the metal.

We note that we did observe an increase in G in CTAB-capped gold interfaces when the gold was modeled with polarizable atoms. To further examine this phenomenon, we have computed the charge density as a function of z for planar systems which contain CTAB or high density MTAB, shown in Figure 11.

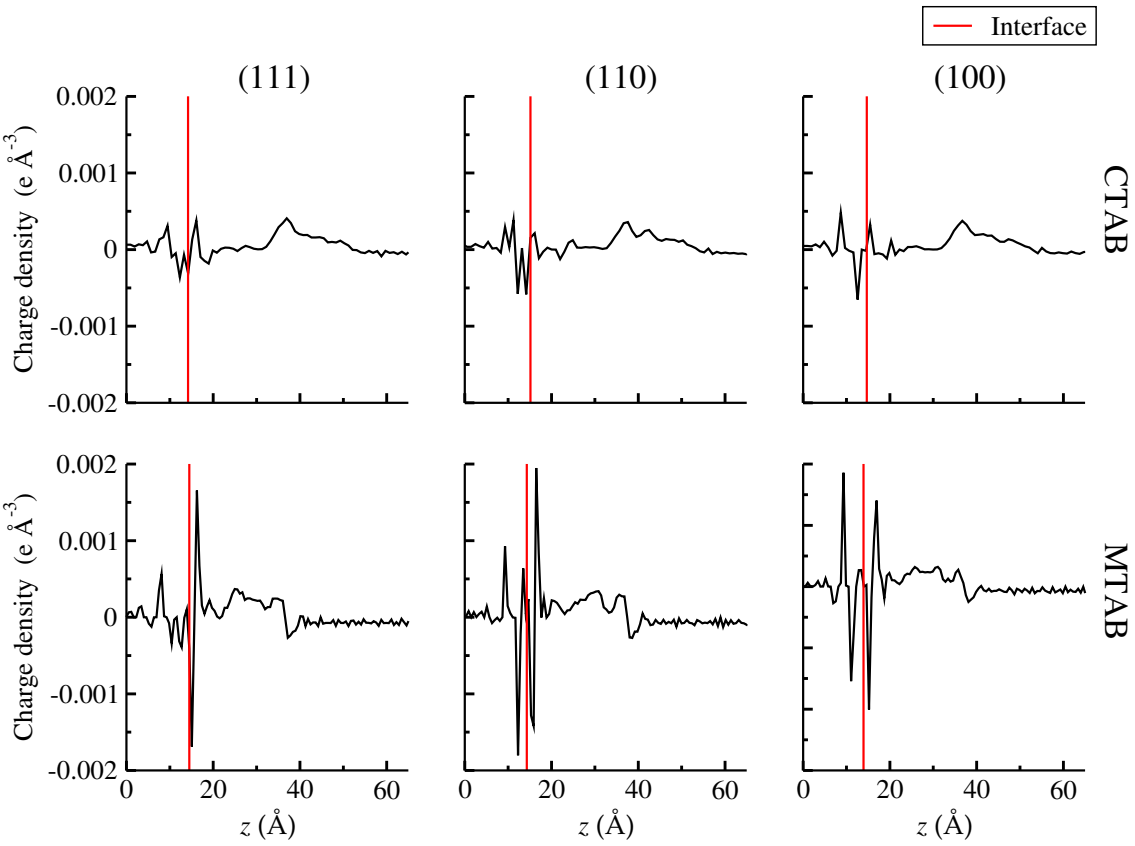

Figure 11: Charge density as a function of z for planar systems containing CTAB (top) or high density MTAB (bottom) with polarizable gold. The red line indicates the interface between gold and the ligand (the point at which the mass densities of both species are effectively 0). Note that the systems have been re-centered so that the center of each metal structure is located at $z = 0$.

In the CTAB systems, the small positive peak directly adjacent to the interface is due to the amine nitrogen in TAB^+, although the Br^- ion can also be found near the gold surface, so the net charge density from the ligand remains small. The negative peaks on the gold side of the interface are the image charge response of the gold surface to the external positive layer of charge. Notably, the (111) and (110) facets contain two adjacent negative image charge peaks indicating that the charge polarization extends two metal layers (~ 4 Å) into the surface. Positive polarization occurs in the layer below this, where again it is represented by two adjacent positive peaks in the (110) facet.

In the MTAB systems, the twinned positive and negative peaks adjacent to the interface are due to a small number of Br^- ions and water molecules adsorbed close to the surface. We observe alternating polarization of the gold layers in response to the presence of the surface-adjacent species, and this polarization extends to an additional two layers below. We also note that the magnitudes of all charge density peaks in the MTAB systems are significantly larger than those in the CTAB systems. The CTAB ligands are not bound strongly to the gold and are free to adopt more diffuse configurations over time, distributing the effect of local polarization. Conversely, the MTAB ligands are anchored to the gold via the S-Au bond and trap local pockets of Br^- ions and water molecules, creating significant charge perturbations adjacent to the surface.

Although the CTAB's binding motif includes a monolayer with two ions in close proximity to the gold, this does not produce a large perturbation of localized charge in the metal surface. In other studies with small ionic surfactants (sodium citrate) or ligands which permit significant water penetration close to the surface (thiolated PEG), the charge densities were between $5-10$ times larger than those observed here.[49,50,59] It appears that water polarization of the surface is a significant contributor to this effect. This polarization could also be enhancing the gold–ligand coupling in the MTAB systems, leading to the large thermal conductance across this interface.

Conclusions

We have examined the differences in thermal conductance across gold interfaces functionalized with both CTAB and MTAB at reasonable surface densities for nanoparticle synthesis. We studied the effects of gold facet, curvature (where possible), and polarizability, as well as ligand identity and packing density in MTAB. Our primary finding is that G is higher in systems capped with MTAB rather than CTAB, likely due to the metal-to-sulfur bond present between MTAB and gold. Conversely, CTAB is a barrier to heat transfer relative to the bare metal interface, in addition to its known cytotoxicity. Factors such as metal polarizability are significant only in the systems capped with CTAB, suggesting that they dominate G only in the absence of strong metal-to-ligand

coupling. Analysis of orientational order parameters revealed that while the higher density MTAB ligands are orientationally ordered but not aligned with the surface normal, the molecular director axis in lower density MTAB ligands is perpendicular to the gold surface. The diffuse mismatch model (DMM) and vibrational densities of states are not predictive of larger trends in thermal conductance in these systems, and it is instead the physical contact between the ligand and solvent, as measured by density overlap statistics, that correlates most strongly the interfacial thermal conductance. We also determined that the magnitude of excess charge density is larger in the high density MTAB systems than in systems containing CTAB. If the goal is for a water solubile, biocompatible ligand with a high degree of thermal conductance to the surrounding medium, a low density MTAB surfactant would appear to be a reasonable choice.

Data and Software Availability

The data used in this study (force field parameters, initial configurations, scripts and meta-data) are available at DOI: 10.5281/zenodo.14232345 Many of the parameters and details are also reproduced in a human-readable format in the Supporting Information. All simulations utilized the OpenMD molecular dynamics engine (See github.com/OpenMD/OpenMD),[54] which is available under a BSD 3-clause license . All analysis tools utilized here have been built-in to OpenMD.

Acknowledgement

Support for this project was provided by the National Science Foundation under grant CHE-1954648. Computational time was provided by the Center for Research Computing (CRC) at the University of Notre Dame.

Supporting Information Available

Details regarding system composition, force field parameters, additional thermal and local mass density profiles, and more information regarding system equilibration described in this work.

Author Contributions

This work was made available through contributions from both authors. Portions of this work are also included in the PhD dissertation of S.A.S.[50] which is available at DOI: 10.7274/25571514 Both authors have approved the final version of the manuscript. S.A.S. and J.D.G. conceived and designed the simulations; S.A.S. performed the simulations; S.A.S. and J.D.G. analyzed the data; S.A.S. and J.D.G. wrote and edited the manuscript. J.D.G. secured financial support for the research.

Notes

The authors declare no competing financial interest.

References

(1) Abdullah, A.; Altaf, M.; Khan, H. I.; Khan, G. A.; Khan, W.; Ali, A.; Bhatti, A. S.; Khan, S. U.; Ahmed, W. Facile room temperature synthesis of multifunctional CTAB coated gold nanoparticles. *Chem. Phys.* **2018**, *510*, 30–36.

(2) Khan, Z.; Singh, T.; Hussain, J. I.; Hashmi, A. A. Au(III)–CTAB reduction by ascorbic acid: Preparation and characterization of gold nanoparticles. *Colloids Surf. B* **2013**, *104*, 11–17.

(3) Nejati, K.; Dadashpour, M.; Ghairibi, T.; Mellatyar, H.; Akbarzadeh, A. Biomedical Applications of Functionalized Gold Nanoparticles: A Review. *J. Clust. Sci.* **2021**, *33*, 1–16.

(4) Tiwari, P. M.; Vig, K.; Dennis, V. A.; Singh, S. R. Functionalized Gold Nanoparticles and Their Biomedical Applications. *Nanomater.* **2011**, *1*, 31–63.

(5) Glomm, W. R. Functionalized Gold Nanoparticles for Applications in Bionanotechnology. *J. Dispers. Sci. Technol.* **2005**, *26*, 389–414.

(6) Almeida, M. B.; Galdiano, C. M. R.; Silva Benvenuto, F. S. R. d.; Carrilho, E.; Brazaca, L. C. Strategies Employed to Design Biocompatible Metal Nanoparticles for Medical Science and Biotechnology Applications. *ACS Applied Materials & Interfaces* **2024**, *0*, in press, DOI: 10.1021/acsami.4c00838.

(7) Cheraghipour, E.; Tamaddon, A.; Javadpour, S.; Bruce, I. PEG conjugated citrate-capped magnetite nanoparticles for biomedical applications. *J. Magn.* **2013**, *328*, 91–95.

(8) Raji, V.; Kumar, J.; Rejiya, C.; Shenoi, M. V. V. N.; Abraham, A. Selective photothermal efficiency of citrate capped gold nanoparticles for destruction of cancer cells. *Exp. Cell Res.* **2011**, *317*, 2052–2058.

(9) Vechia, I. C. D.; Steiner, B. T.; Freitas, M. L.; dos Santos Pedroso Fidelis, G.; Galvani, N. C.; Ronchi, J. M.; Possato, J. C.; Ívens Fagundes, M.; Rigo, F. K.; Feuser, P. E.; de Araújo, P. H. H.; de Ávila, R. A. M. Comparative cytotoxic effect of citrate-capped gold nanoparticles

with different sizes on noncancerous and cancerous cell lines. *J. Nanopart. Res.* **2020**, *22*, 133.

(10) Mirkin, C. A.; Letsinger, R. L.; Mucic, R. C.; Storhoff, J. J. A DNA-based method for rationally assembling nanoparticles into macroscopic materials. *Nature* **1996**, *382*, 1–23.

(11) Zhang, X.; Servos, M. R.; Liu, J. Instantaneous and Quantitative Functionalization of Gold Nanoparticles with Thiolated DNA Using a pH-Assisted and Surfactant-Free Route. *J. Am. Chem. Soc.* **2012**, *134*, 7266–7269.

(12) Peng, C.; Yu, M.; Zheng, J. In Situ Ligand-Directed Growth of Gold Nanoparticles in Biological Tissues. *Nano Lett.* **2020**, *20*, 1378–1382.

(13) Sibuyi, N. R. S.; Moabelo, K. L.; Fadaka, A. O.; Meyer, S.; Onani, M. O.; Madiehe, A. M.; Meyer, M. Multifunctional Gold Nanoparticles for Improved Diagnostic and Therapeutic Applications: A Review. *Nanoscale Res. Lett.* **2021**, *16*, 1–27.

(14) Lee, J.-W.; Soonsanga, S.; Helmann, J. D. A complex thiolate switch regulates the Bacillus-subtilisorganic peroxide sensor OhrR. *PNAS* **2007**, *4*, 8743–8748.

(15) Wang, S.; Lu, W.; Tovmachenko, O.; Rai, U. S.; Yu, H.; Ray, P. C. Challenge in understanding size and shape dependent toxicity of gold nanomaterials in human skin keratinocytes. *Chem. Phys. Lett.* **2008**, *463*, 145–149.

(16) Jia, Y. P.; Shi, K.; Liao, J. F.; Peng, J. R.; Hao, Y.; Qu, Y.; Chen, L. J.; Liu, L.; Yuan, X.; Qian, Z. Y.; Wei, X. W. Effects of Cetyltrimethylammonium Bromide on the Toxicity of Gold Nanorods Both In Vitro and In Vivo: Molecular Origin of Cytotoxicity and Inflammation. *Small Methods* **2020**, *4*, 1900799.

(17) Carnovale, C.; Bryant, G.; Shukla, R.; Bansal, V. Identifying Trends in Gold Nanoparticle Toxicity and Uptake: Size, Shape, Capping Ligand, and Biological Corona. *ACS Omega* **2019**, *4*, 242–256.

(18) Zarska, M. et al. Biological safety and tissue distribution of (16-mercaptohexadecyl) trimethylammonium bromide-modified cationic gold nanorods. *Biomater.* **2018**, *154*, 275–290.

(19) Vigderman, L.; Manna, P.; Zubarev, E. R. Quantitative Replacement of Cetyl Trimethylammonium Bromide by Cationic Thiol Ligands on the Surface of Gold Nanorods and Their Extremely Large Uptake by Cancer Cells. *Angew. Chem.* **2012**, *124*, 660–665.

(20) Salajkova, S.; Havel, F.; Sramek, M.; Novotny, F.; Malinak, D.; Dolezal, R.; Prchal, L.; Benkova, M.; Soukup, O.; Musilek, K.; Kuca, K.; Bartek, J.; Proska, J.; Zarska, M.; Hodny, Z. The Effect of Chemical Structure of OEG Ligand Shells with Quaternary Ammonium Moiety on the Colloidal Stabilization, Cellular Uptake and Photothermal Stability of Gold Nanorods. *Int. J. Nanomedicine* **2021**, *16*, 3407–3427.

(21) Wu, M.; Vartanian, A. M.; Chong, G.; Pandiakumar, A. K.; Hamers, R. J.; Hernandez, R.; Murphy, C. J. Solution NMR Analysis of Ligand Environment in Quaternary Ammonium-Terminated Self-Assembled Monolayers on Gold Nanoparticles: The Effect of Surface Curvature and Ligand Structure. *J. Am. Chem. Soc.* **2019**, *141*, 4316–4327.

(22) Liang, D.; Dahal, U.; Wu, M.; Murphy, C. J.; Cui, Q. Ligand Length and Surface Curvature Modulate Nanoparticle Surface Heterogeneity and Electrostatics. *J. Phys. Chem. C* **2020**, *124*, 24513–24525.

(23) Ali, M. R.; Wu, Y.; El-Sayed, M. A. Gold-Nanoparticle-Assisted Plasmonic Photothermal Therapy Advances Toward Clinical Application. *J. Phys. Chem. C* **2019**, *123*, 15375–15393.

(24) Huang, J.; Park, J.; Wang, W.; Murphy, C. J.; Cahill, D. G. Ultrafast Thermal Analysis of Surface Functionalized Gold Nanorods in Aqueous Solution. *ACS Nano* **2013**, *7*, 589–597.

(25) Hu, M.; Hartland, G. V. Heat Dissipation for Au Particles in Aqueous Solution: Relaxation Time versus Size. *J. Phys. Chem. B* **2002**, *106*, 7029–7033.

(26) Nguyen, S. C.; Zhang, Q.; Manthiram, K.; Ye, X.; Lomont, J. P.; Harris, C. B.; Weller, H.; Alivisatos, A. P. Study of Heat Transfer Dynamics from Gold Nanorods to the Environment via Time-Resolved Infrared Spectroscopy. *ACS Nano* **2016**, *10*, 2144–2151.

(27) Kawasaki, H.; Nishimura, K.; Arakawa, R. Influence of the Counterions of Cetyltrimetylammonium Salts on the Surfactant Adsorption onto Gold Surfaces and the Formation of Gold Nanoparticles. *J. Phys. Chem. C* **2007**, *111*, 2683–2690.

(28) Meena, S. K.; Sulpizi, M. Understanding the Microscopic Origin of Gold Nanoparticle Anisotropic Growth from Molecular Dynamics Simulations. *Langmuir* **2013**, *29*, 14954–14961.

(29) da Silva, J. A.; Dias, R. P.; da Hora, G. C. A.; Soares, T. A.; Meneghetti, M. R. Molecular Dynamics Simulations of Cetyltrimethylammonium Bromide (CTAB) Micelles and their Interactions with a Gold Surface in Aqueous Solution. *J. Braz. Chem. Soc.* **2018**, *29*, 191–199.

(30) Kalipillai, P.; Raghuram, E.; Bandyopadhyay, S.; Mani, E. Self-assembly of a CTAB surfactant on gold nanoparticles: a united-atom molecular dynamics study. *Phys. Chem. Chem. Phys.* **2022**, *24*, 28353–28361.

(31) Chen, X.; Munjiza, A.; Zhang, K.; Wen, D. Molecular Dynamics Simulation of Heat Transfer from a GoldNanoparticle to a Water Pool. *J. Phys. Chem. C* **2014**, *118*, 1285–1293.

(32) Puliti, G.; Paolucci, S.; Sen, M. Thermodynamic properties of gold–water nanolayer mixtures using molecular dynamics. *J. Nanopart. Res.* **2011**, *13*, 4277–4293.

(33) Wilson, B. A.; Nielsen, S. O.; Randrianalisoa, J. H.; Qin, Z. Curvature and temperature-dependent thermal interface conductance between nanoscale gold and water. *J. Chem. Phys.* **2022**, *157*, 054703.

(34) Paniagua-Guerra, L. E.; Ramos-Alvarado, B. Thermal transport across flat and curved gold-

water interfaces: Assessing the effects of the interfacial modeling parameters. *J. Chem. Phys.* **2023**, *158*, 134717.

(35) Gutiérrez-Varela, O.; Merabia, S.; Santamaria, R. Size-dependent effects of the thermal transport at gold nanoparticle-water interfaces. *J. Chem. Phys.* **2022**, *157*, 084702.

(36) Wu, X.; Ni, Y.; Zhu, J.; Burrows, N. D.; Murphy, C. J.; Dumitrica, T.; Wang, X. Thermal Transport across Surfactant Layers on Gold Nanorods inAqueous Solution. *ACS Appl. Mater. Interfaces* **2016**, *8*, 10581–10589.

(37) Kuang, S.; Gezelter, J. Velocity shearing and scaling RNEMD: a minimally perturbing method for simulating temperature and momentum gradients. *Mol. Phys.* **2012**, *110:9-10*, 691–701.

(38) Stocker, K.; Gezelter, J. A Method for Creating Thermal and Angular Momentum Fluxes in Nonperiodic Simulations. *J. Chem. Theory Comput.* **2014**, *10*, 1878–1886.

(39) Ríos-López, M.; Mendez-Bermúdez, J. G.; Vázquez-Sánchez, M. I.; Domínguez, H. Surface tension calculations of the cationic (CTAB) and the zwitterionic (SB3-12) surfactants using new force field models: a computational study. *Mol. Phys.* **2019**, *117*, 3632–3641.

(40) Lubna, N.; Kamath, G.; Potoff, J. J.; Rai, N.; Siepmann, J. I. Transferable Potentials for Phase Equilibria. 8. United-Atom Description for Thiols, Sulfides, Disulfides, and Thiophene. *J. Phys. Chem. B* **2005**, *109*, 24100–24107.

(41) Stubbs, J. M.; Potoff, J. J.; Siepmann, J. I. Transferable Potentials for Phase Equilibria. 6. United-Atom Description for Ethers, Glycols, Ketones, and Aldehydes. *J. Phys. Chem. B* **2004**, *108*, 17596–17605.

(42) Jorgensen, W. L.; Maxwell, D. S.; Tirado-Rives, J. Development and Testing of the OPLS All-Atom Force Field on Conformational Energetics and Properties of Organic Liquids. *J. Am. Chem. Soc.* **1996**, *118*, 11225–11236.

(43) Weiner, S. J.; Kollman, P. A.; Nguyen, D. T.; Case, D. A. An all atom force field for simulations of proteins and nucleic acids. *J. Comp. Chem.* **1986**, *7*, 230–252.

(44) Martin, M. G.; Siepmann, J. I. Transferable Potentials for Phase Equilibria. 1. United-Atom Description of n-Alkanes. *J. Phys. Chem. B* **1998**, *102*, 2569–2577.

(45) Schapotschnikow, P.; Pool, R.; Vlugt, T. J. H. Selective adsorption of alkyl thiols on gold in different geometries. *Comp. Phys. Comm.* **2007**, *177*, 154–157.

(46) Pool, R.; Schapotschnikow, P.; Vlugt, T. J. H. Solvent Effects in the Adsorption of Alkyl Thiols on Gold Structures: A Molecular Simulation Study. *J. Phys. Chem. C* **2007**, *111*, 10201–10212.

(47) Bhattarai, H.; Newman, K.; Gezelter, J. Polarizable potentials for metals: The density readjusting embedded atom method (DR-EAM). *Phys. Rev. B* **2019**, *99*, 094106.

(48) Bhattarai, H.; Newman, K.; Gezelter, J. The role of polarizability in the interfacial thermal conductance at the gold-water interface. *J. Chem. Phys.* **2020**, *153*, 204703.

(49) Shavalier, S. A.; Gezelter, J. D. Thermal Transport in Citrate-Capped Interfaces Using a Polarizable Force Field. *J. Phys. Chem. C* **2022**, *126*, 12742–12754.

(50) Shavalier, S. A. Reverse non-equilibrium molecular dynamics simulations of thermal transport through functionalized gold interfaces. PhD dissertation, University of Notre Dame, Notre Dame, Indiana, 2024.

(51) Zhou, X.; Johnson, R.; Wadley, H. Misfit-energy-increasing dislocations in vapor-deposited CoFe/NiFe multilayers. *Phys. Rev. B* **2004**, *69*, 144113.

(52) Berendsen, H.; Grigera, J.; Straatsma, T. The Missing Term in Effective Pair Potentials. *J. Phys. Chem.* **1987**, *91*, 6269–6271.

(53) Dou, Y.; Zhigilei, L. V.; Winograd, N.; Garrison, B. J. Explosive Boiling of Water Films Adjacent to Heated Surfaces: A Microscopic Description. *J. Phys. Chem. A* **2001**, *105*, 2748–2755.

(54) Drisko, C. R.; Bhattarai, H.; Fennell, C. J.; Stocker, K. M.; Vardeman, C. F.; Gezelter, J. D. OpenMD: A parallel molecular dynamics engine for complex systems and interfaces. *Journal of Open Source Software* **2024**, *9*, 7004, DOI: 10.21105/joss.07004.

(55) Martínez, L.; Andrade, R.; Birgin, E.; Martínez, J. Packmol: A package for building initial configurations for molecular dynamics simulations. *J. Chem. Comput.* **2009**, *30(13)*, 2157–2164.

(56) Vardeman, C. F.; Stocker, K. M.; Gezelter, J. D. The Langevin Hull: Constant Pressure and Temperature Dynamics for Nonperiodic Systems. *J. Chem. Theory Comput.* **2011**, *7*.

(57) Römer, F.; Lervik, A.; Bresme, F. Nonequilibrium molecular dynamics simulations of the thermal conductivity of water: A systematic investigation of the SPC/E and TIP4P/2005 models. *J. Chem. Phys.* **2012**, *137*, 074503, DOI: 10.1063/1.4739855.

(58) Armstrong, J.; Lervik, A.; Bresme, F. Enhancement of the Thermal Polarization of Water via Heat Flux and Dipole Moment Dynamic Correlations. *J. Phys. Chem. B* **2013**, *117*, 14817–14826.

(59) Shavalier, S. A.; Gezelter, J. D. Heat Transfer in Gold Interfaces Capped with Thiolated Polyethylene Glycol: A Molecular Dynamics Study. *J. Phys. Chem. B* **2023**, *127*, 10215–10225.

(60) Pandey, H. D.; Leitner, D. M. Thermalization and Thermal Transport in Molecules. *J. Phys. Chem. Lett.* **2016**, *7*, 5062–5067.

(61) Swartz, E.; Pohl, R. Thermal boundary resistance. *Rev. Mod. Phys.* **1989**, *61*, 605–668.

(62) Monachon, C.; Weber, L.; Dames, C. Thermal Boundary Conductance: A Materials Science Perspective. *Annu. Rev. Mater. Res.* **2016**, *46*, 433–463.

(63) Stocker, K. M.; Neidhart, S. M.; Gezelter, J. D. Interfacial thermal conductance of thiolate-protected gold nanospheres. *J. Appl. Phys.* **2016**, *119*, 025106.

TOC Graphic